



HAL
open science

Corrosion of carbon steel in clay compact environments at 90 °C: Effect of confined conditions

M.L. Schlegel, F. Martin, M. Fenart, C. Blanc, J. Varlet, E. Foy

► To cite this version:

M.L. Schlegel, F. Martin, M. Fenart, C. Blanc, J. Varlet, et al.. Corrosion of carbon steel in clay compact environments at 90 °C: Effect of confined conditions. *Corrosion Science*, 2021, 184, pp.109368. 10.1016/j.corsci.2021.109368 . cea-03748896

HAL Id: cea-03748896

<https://cea.hal.science/cea-03748896>

Submitted on 22 Mar 2023

HAL is a multi-disciplinary open access archive for the deposit and dissemination of scientific research documents, whether they are published or not. The documents may come from teaching and research institutions in France or abroad, or from public or private research centers.

L'archive ouverte pluridisciplinaire **HAL**, est destinée au dépôt et à la diffusion de documents scientifiques de niveau recherche, publiés ou non, émanant des établissements d'enseignement et de recherche français ou étrangers, des laboratoires publics ou privés.



Distributed under a Creative Commons Attribution - NonCommercial 4.0 International License

1 **Corrosion of carbon steel in clay compact environments at**
2 **90 °C: effect of confined conditions**
3

4 M. L. Schlegel¹, F. Martin², M. Fenart², C. Blanc¹, J. Varlet¹, E. Foy³

5 1 Université Paris Saclay, CEA, Service d'Études Analytiques et de Réactivité des Surfaces, 91191, Gif-
6 sur-Yvette, France.

7 2 Université Paris Saclay, CEA, Service de Corrosion et du Comportement des Matériaux dans leurs
8 Environnements, 91191, Gif-sur-Yvette, France

9 3 LAPA-IRAMAT, NIMBE, CEA, CNRS, Université Paris Saclay, CEA Saclay, F-91191 Gif-sur-
10 Yvette, France

11 **Abstract**

12 Corrosion of low alloy carbon steel in simulated crevices and in a perforated envelope containing a
13 rod, mimicking the liner-overpack system, was assessed at 90 °C in anoxic water-saturated clay.
14 Corrosion in crevices was limited (< 1 µm/year). The corroded surface exposed magnetite with a fringe
15 of siderite. Internal corrosion of the envelope was heterogeneous due to gradual filling with porewater,
16 and average corrosion depth for the internal rod was limited to 11.5 µm after 76 months. Magnetite was
17 the main corrosion product replacing steel, together with chukanovite, Fe silicate, and outer siderite in
18 areas first bathed with porewater.

19 **Keywords**

20 Carbon steel (A) ; Clay (A); SEM (B) ; XRD (B) ; Raman spectroscopy (B)

21

22 1 Introduction

23 Decades of investigation on the management of high-level radioactive waste (HLW) established
24 disposal in geologic repositories as the safest and most sustainable approach to deal with this legacy of
25 nuclear industry [1-3]. In these disposal facilities, confinement of HLW is imparted to metallic canisters
26 embedded in bentonite, clay, or concrete barriers [4, 5]. For example, the early French project for a deep
27 underground disposal [6] relied on encapsulation of nuclear glass in stainless steel containers and low-
28 alloy steel (C-steel) overpacks inserted in steel-lined boreholes within the Callovo-Oxfordian claystone
29 (Cox) of the geologic repository (Figure 1a). The liner was meant to keep the borehole circular, should
30 the waste package be retrieved in any far future. It was not designed for tightness, and so porewater, first
31 filling the space between the liner and clay (Figure 1b), would later seep in, and lead to corrosion in a
32 confined space gradually filled up with a reactive anoxic solution (Figure 1c). Thus, knowledge on the
33 corrosion processes occurring under such confined conditions (i.e. where the reacting surface is
34 surrounded by metal walls and sides, as opposed to surfaces plainly exposed to the clay matrix) was
35 deemed mandatory.

36 A considerable number of studies have dealt with corrosion under HLW disposal conditions.
37 Experiments were performed in laboratories [7-24], either on compact systems with a water flow, or in
38 solutions or slurries with a reasonably high surface of steel exposed to water. These short-term (usually
39 less than 10 years) laboratory studies were complemented by *in situ* investigations in deep underground
40 laboratories [25-29], and by analyses of archaeological artefacts [30-36] or meteorites [37]. Surprisingly,
41 little attention was devoted to the impact of partially confined anoxic conditions. Yet, in partially
42 confined conditions, the solution composition is expected to be controlled by the interplay between slow
43 diffusive or advective transport and corrosion/alteration reactions. The same limitations on transport are
44 expected to affect the formation and corrosion in steel cracks and crevices. Finally, the impact of gradual
45 filling has been entirely unexplored.

46 The present study focuses on the corrosion of C-steel in two examples of confined environments. One
47 corresponds to a simulated crevice between two C-steel rods, a situation encountered either between
48 two liner sections or for hypothetical overpack crevices. In this case, porewater should diffuse along

49 the crevice surface. The other case corresponds to an end-sealed, perforated C-steel tube (envelope)
50 containing a C-steel rod, in order to simulate the situation where porewater would reach the overpack
51 through the liner after clay percolation. In that case, porewater renewal is limited by transport through
52 holes in the envelope. These specimens were reacted for more than six years at 90 °C (the peak
53 temperature expected for the repository) under anoxic conditions in water-saturated Cox in a dedicated
54 setup [38], under constant slow flux of water in equilibrium with clay. These experiments extend and
55 complete previous observations made on shorter time scales [39]. Corrosion damage was assessed by
56 weight loss, and the nature and distribution of corrosion products (CPs) by microscale investigations.
57 The results show how the respective kinetics of transport and precipitation of porewater solutes within
58 confined spaces results in CPs heterogeneity, ultimately controlling the formation of protective layers
59 under anoxic clay conditions.

60 **2 Materials and methods**

61 ***2.1 Experimental setup***

62 The experimental setup has been detailed in a companion paper [38]. Briefly, samples of A37 C-steel
63 with various geometries were inserted in cylindrical Cox bricks within high-pressure cells (Figure 2a),
64 fed with anoxic synthetic clay porewater [12], and heated at 90 °C for several months to years. Three
65 types of sample geometries were investigated. Type 1 was a massive rod (diameter 10 mm, length 30
66 mm), the steel-clay interface of which was already investigated [38]. Type 2 was made of two head-on
67 short rods (lengths of 14 and 15 mm) separated by a polytetrafluoroethylene (PTFE) disk (9 mm
68 diameter, 1 mm thickness), and was designed to investigate corrosion in a crevice configuration (Figure
69 2b). Type 3 was made of an A37 tube with welded lids (length 30 mm, outer diameter 16 mm), pierced
70 with six 2 mm-diameter holes and containing an A37 rod (diameter 8 mm, length 20 mm) centered with
71 PTFE rings (Figure 1b,c). The rings prevented any contact between the internal rod and the tube or lids,
72 and so hindered galvanic coupling. These specimens, thereafter referred to as “cover integrity loss”
73 (CIL), were investigated to understand corrosion in confined volumes (Figure 1a, bottom right). These
74 volumes differ from the simulated crevices by the greater metal-to metal distance (3 mm). Samples were
75 collected after given exposure times (7, 15, 27, 40 and 76 months). One type 2 sample was quickly saved

76 in a glove box for characterization, and the others were used for gravimetric assessment of the average
77 corrosion depth. In the case of the CIL specimens, only the internal rod were used for gravimetric
78 measurements, and only specimens for 40 and 76 months were kept for microcharacterization.

79 **2.2 Sample preparation and microcharacterization**

80 Samples saved for microcharacterization were impregnated with resin, sectioned, and the cross-
81 sections polished down to 1 μm using diamond paste, as described elsewhere [38]. Thin sections for
82 transmission micro X-ray diffraction (μXRD) were obtained by polishing thin slices down to 100 μm
83 thickness, and mounted on a sample holder under anoxic conditions [28, 29].

84 Optical images and micro Raman (μRaman) spectra were collected on cross-sections kept in airtight
85 boxes with a glass window. Microphotographies were obtained with an Olympus BX51M equipped with
86 a CCD camera (Sony Exwave HAD) and operated with the analySIS software. Micro Raman
87 spectroscopy (μRS) was carried out on microspectrometers (Renishaw Invia and LabRam HR800) with
88 excitation wavelengths of 532 or 785 nm and low power outputs ($\geq 500 \mu\text{W}$) to avoid solid overheating.
89 Scanning electron microscopy (JEOL JSM7000-F) was performed on carbon-coated samples at 10 kV
90 and 1.6-2 nA. Energy-Dispersive X-ray (EDX) spectra were collected on Points of Interest (PI) with a
91 silicon-drift detector (Bruker XFlash 5010) and processed as described elsewhere [38]. Quantifications
92 are given in atomic percent (at.%), and are rounded to two significant digits in the text. Elemental maps
93 were recorded by sample continuous scanning and adding the EDX raw counts on each pixel. The μXRD
94 data were recorded in transmission mode, with a Mo $\text{K}\alpha$ rotating anode source (wavelength of 0.70932
95 nm), a focused X-ray beam (30 \times 50 μm , vertical \times horizontal), and a 2D Image plate detector (GE
96 Healthcare).

97 **3 Results**

98 **3.1 Weight loss**

99 Figure 3 shows the evolution of the average corrosion depth with reaction time for half-rods
100 mimicking a crevice (Figure 3a), and for the CIL internal rod (Figure 3b). The average corrosion depth

101 for the half-rods (crevice configuration) equals $10.5 \pm 2.2 \mu\text{m}$ after seven months of corrosion. It then
102 increases at a constant rate, up to $25.4 \pm 2.2 \mu\text{m}$ after 76 months of reaction. This trend was tentatively
103 fitted by linear, power, or logarithmic laws. As previously observed [38], the logarithmic law yielded the
104 worst agreement and was discarded. The linear law provided a good estimate of the long-term trend,
105 avoiding to take into account the initial, probably high corrosion rate, and could be described by:

$$106 \quad D_{CLL} = 8.7 (\pm 2.1) + 3.2 (\pm 0.8) \times t, \quad (1)$$

107 where D_{CLL} is the average corrosion depth for crevice samples (in μm) and t is the exposure time (in
108 years).

109 The linear corrosion rate ($3.2 \pm 0.8 \mu\text{m}/\text{year}$) compares with the value obtained for massive rods in
110 contact with clay ($3.5 \mu\text{m}/\text{year}$; [38]). Because about 87 % of the half-rod is in contact with clay, the
111 similarity in rates suggests that damage in the simulated crevice is probably limited. At the highest, it
112 would be of about the same order of magnitude as for the steel-clay interface. Optical microscope and
113 SEM observations of the crevice mouths beneath and around the PTFE disc did not reveal any localized
114 corrosion features.

115 For the internal rod of the CIL specimen, the average corrosion depth is more limited for short reaction
116 times (3.3 and $5 \pm 1 \mu\text{m}$ at 7 and 27 months of reaction, respectively), probably due to delays needed by
117 pore water to reach the internal rod itself. The long-term trend is blurred by the scatter between the
118 values measured after 40 months of reaction ($17.5 \mu\text{m}$) and at the end of the experiment ($11.5 \mu\text{m}$ at 76
119 months of reaction). This difference is larger than the estimated uncertainty in measurements ($\pm 1 \mu\text{m}$).
120 Since only one rod was weighted (the other internal rod was kept for analyses), the origin of this scatter
121 is unknown. Nevertheless applying the affine relationship on these points yields:

$$122 \quad D_{\mu CLL} = 1.8 (\pm 4.8) + 2.0 (\pm 1.6) \times t. \quad (2)$$

123 As expected from the scatter in values of average corrosion depths, parameters are affected by large
124 uncertainties. However, most of the scatter is due to a single outlier at 40 months.

125 **3.2 Microstructural characterization**

126 3.2.1 Corrosion at simulated crevices

127 Electron micrographs show that corrosion within the simulated crevices is generally very limited,
128 with little roughening of the metal surface (Figure 4) and depressions shallower than 20 μm . The
129 corroded steel is covered by thin layers of CPs, with a thickness of less than 5 μm . This layer is compact
130 and usually tightly bound to the metal surface. For short exposure times (7 to 27 months), the layer is
131 homogeneous, with a composition dominated by O (74-78 at.%), Mg (1.2-12 at.%), Ca (0.4-6.3 at.%),
132 and Fe (14-19 at.%). The cationic composition and the O / (Fe + Mg + Ca) ratios suggest the formation
133 of hydroxylated or carbonated Fe compounds, i.e. (Mg, Ca)-doped siderite (ankerite). Locally, a slight
134 enrichment in Si could be observed (up to 4 at.%), possibly related to the presence of Fe silicate. The
135 presence of Mg, Ca and Si demonstrates that clay porewater with dissolved elements has been
136 percolating along the crevice. For higher exposure durations (≥ 40 months), two successive layers are
137 present (Figure 5). The inner layer contains essentially O, Fe, and Si, with a small amount of S. The
138 composition of this inner layer (11-15 at.% Si, 23-28% Fe, 58-59 at.% O, 1.1-1.4 at.% S; Table 2, PI 1-3)
139 suggests the formation of mostly Fe silicate phase. The outer layer (Table 2, PI 4-6) has a composition
140 comparable to that of the early CPs, and is made of ankerite, as shown by μXRD performed on a thin
141 slice (b). In conclusion, the nature of the CPs in the crevice indicated that corrosion, albeit much limited
142 compared to steel surfaces in direct contact with clay, occurred in presence of porewater.

143 3.2.2 Corrosion inside the CIL setup

144 That the CIL specimens were only gradually filled by porewater (through the drilled holes in the
145 external tube) is evident from the presence of water marks on the inside and on the internal rods for short
146 exposure times (e.g. 15 months; Figure 6a). For longer exposure times, these marks are no longer
147 observed (Figure 6b), attesting to a complete filling of the tube with solution. Cross-sections show that
148 the inside surface of the tube wall (inside wall) and of the internal rod are heterogeneously corroded
149 (Figure 7a-f). The presence of clay minerals near part of the inside wall is interpreted as resulting from
150 clay penetration and settling. This allows identifying the bottom part of the CIL specimen (Figure 7 a,d).
151 It is then possible to remark that steel damage in the bottom parts (up to 100 μm after 40 months; Figure

152 7a) is more important than on the upper parts (up to 35 μm after 76 months; Figure 7f). This suggests
153 that the lower and upper inside walls experienced distinct conditions, in line with immersion of the lower
154 wall occurring first. According to SEM cross-sections examined along the lower inside wall, corrosion
155 depth is usually found around 35-40 μm , locally as deep as 100 μm after 40 months exposure. Corrosion
156 is comparatively more limited on the upper inside wall, with 25 μm on average and locally as deep as 60
157 μm after 76 months (Figure 7c,f). The corrosion of the internal rod is intermediate in nature and
158 magnitude between those of the upper and lower walls (Figure 7b,e). The average corroded metal depth
159 from SEM analyses equals about 10 μm and 5 μm after 40 and 76 months exposure, respectively. Some
160 straight-faced depressions as deep as 20 μm are visible along the interface, which may correspond to
161 local higher oxidation rates associated with favourable orientation of steel grains.

162 The steel-CPs interface is significantly jagged, attesting to the heterogeneous nature of the corrosion
163 interface. Nonetheless, no specific feature of any localized corrosion process (intergranular oxidation or
164 pitting) is observed. In addition, for all interfaces, several successive units of CPs can be identified. The
165 innermost layer of CPs forms at the expense of metal; hence, it corresponds to a Dense Products Layer
166 (DPL). The trace of the metal initial surface is visualised by a discontinuous median corrosion layer
167 (MCL), with a thickness of a few μm . A layer of outer corrosion products (OCPs) can then be observed
168 with contrasted morphologies, either as CPs mixed with clay (Figure 7a,d), or as massive layers (Figure
169 7b,c,e,f), sometimes protruding outer filamentous crystallites (Figure 7b,c). The nature of the CPs units
170 has been thoroughly investigated to understand the control of corrosion reactions in the liner-overpack
171 interspace.

172 Chemical mapping (Figure 8.a) and quantitative analysis (Table 3) of the lower inside wall after 40
173 months of exposure show that the DPL essentially contains O and Fe (Table 3, PI-1-6), with a significant
174 local enrichment in Si for the DPL most external fringe (up to 20 at.%; Table 3, PI 5-6). Detailed
175 analysis shows the coexistence of three types of crystalline solids. The first type has a very high Fe
176 content and comparatively low O content (40-44 and 54-55 at.% respectively ; Table 3, PI 1-2) and is
177 identified by μRS as magnetite (Figure 8.b, PI a,b). The second type has a lower Fe content and a higher
178 O content (33-35 and 62-63 at.% respectively; Table 3, PI 3-4), and is identified as chukanovite (Figure

179 8.b, PI c). Interestingly, chukanovite is slightly enriched in S (up to 1.2 at.%), a preferential association
180 which was also observed in corrosion layers developed in clayey water [28]. The third type of solid
181 would correspond to Fe silicate phases, for which there is no Raman signal [38]. The trace of the original
182 surface presumably coincides with the Si-enriched thin layer (17-20 at.%). The Fe-rich solids present as
183 outer CPs (OCPs) display measured O/Fe ratios quite comparable to that of magnetite, but due to the
184 heterogeneity and porosity of this layer, the EDX quantification may be unreliable. Local μ Raman
185 spectra showed bands near 250, 300, and 395 cm^{-1} (Figure 8b, PI d), near the positions observed for
186 goethite (α -FeOOH), yet Raman bands at higher wavenumbers expected for goethite were not observed.
187 In fact μ XRD patterns of this area (not shown) suggest the predominance of magnetite and the presence
188 of siderite. Finally, the outermost material is a mixture of clay material cemented by siderite with a
189 remarkably low Ca content (less than 0.6 at.%).

190 On the upper inside wall, after 40 months exposure, an internal (Fe, O) layer is observed with an O/Fe
191 ratio suggesting magnetite (Figure 9 and Table 4, PI 1). An intermediate (Fe, Si, O) layer is also
192 observed, with a Si content of ~17-18 at.% (Figure 9 and Table 4, PI 2 to 4). This layer is in contact with
193 an external Fe-rich layer with locally some Ca (Table 4, PI 5 to 7) suggesting the formation of ankerite.
194 The most external layer has a radial fibrous-like morphology with some round precipitates, and is made
195 of O and Fe (possibly C and H). Insight into the nature of these solids composing the outermost layer
196 was actually obtained from the investigation of the internal rod.

197 After 40 months corrosion, the internal rod displays some depressions filled with magnetite (see
198 μ Raman spectrum at PI a; Figure 10b). The innermost layers in contact with steel contain essentially Fe
199 (29 at.%) and O (67 at.%; Table 5), suggesting an Fe (hydr)oxide or hydroxycarbonate. There is a
200 possibility that this very thin layer extends laterally on the whole metal-oxide interface. The next layer
201 (MCL in Figure 10a) is made of a 7 μm thick Si-rich fringe (Si content between 15 and 17.5 at.%). This
202 layer is in contact with another (Fe, O) unit, the Fe content of which gradually decreases with increasing
203 distance to steel (Table 5, PI 5-8). The Ca content of these layers is quite variable (0.4-6.8 at.%), hinting
204 at the possible local presence of siderite and ankerite. Indeed, μ RS reveal the presence of Fe-rich
205 carbonate (peak near 1088 cm^{-1}), and also of chukanovite (peak near 1071 cm^{-1} ; Figure 10b, PI b).

206 Finally, the most external layer is made of well-separated minerals appearing as filamentous on the
207 cross-section, with an increasing porosity from steel to the environment. Surprisingly, the O:Fe ratio of
208 these minerals, measured by EDXS, is around 55:45, a value typical of magnetite. Locally, these layers
209 contain (Ca, Fe) rich nodules, identified by μ RS as ankerite (Figure 10b, PI c).

210 Similar observations can be made on the nature and distribution of CPs for the 76-months sample
211 (Figure 7d-f). One notable difference is that only magnetite is detected in the DPL layer for all parts of
212 the tube inside walls, as well as for the internal rod. Also, OCPs made of siderite are observed for the
213 lower wall. The upper wall is more corrugated, with enlargement of several oxide penetrations over
214 distances of a few tens of μm (Figure 7f). In addition, the Si-rich fringe on this sample is not continuous,
215 suggesting it has not formed at the same rates on the T40 (40 months) and T76 (76 months) samples, or
216 that it has partially dissolved on the T76 sample. Thus, although the whole inside wall was in contact
217 with solution for more than three years, the discrepancy between the bottom and top part of this wall
218 persisted throughout the exposure time.

219 **4 Discussion**

220 **4.1 Steel corrosion in the crevice configuration**

221 Compared to steel surfaces in direct contact at 80-90 °C with clay [38], bentonite [40], or porewater
222 [27, 28], the corrosion damage in the simulated crevices is quite limited. Even after 76 months of
223 exposure to the media, the thickness of corroded steel and of corrosion layers are both limited to a few
224 μm (Figure 4). The little CPs (a few μm) present within the crevices are made of Fe (hydr)oxide or
225 carbonate, and Fe silicate. The presence of silicate, which could be transported only in dissolved (or
226 colloidal) form, indicates that fluids have penetrated deep in the crevice.

227 One hypothesis for this near-absence of CPs is that the surface does corrode, but that oxidized Fe is
228 transported away by diffusion instead of precipitating *in situ*. In that case, however, corrosion would
229 likely have resulted in greater surface roughening, which is not observed here. Thus, the absence of CPs
230 probably results from limited corrosion, or to limited transport of water and reacting species in the
231 crevice. Under anoxic conditions, a protecting layer would remain stable because of basic pH [41, 42],

232 and of the low concentrations of ligands such as carbonate and silicate. It may however be destabilized
233 by the presence of chloride [43]. In addition, the presence of CPs on the whole crevice surface buffers
234 the concentration of dissolved Fe to the solubility of these solids, thus decreasing lateral gradients and
235 hindering outward transport of Fe. Thus, it seems that the corrosion rate is limited by the slow
236 dissolution rate of the protective CPs, related to rather steady chemical conditions and to a limited
237 ingress of reactive species.

238 Finally, it is worth mentioning that the corrosion mechanism within these model crevices differs from
239 those usually observed in oxic environments, in which a significant oxygen gradient can occur. Such
240 gradients can favor the onset of spatial decoupling between cathodic reactions on the external surfaces
241 near the crevice lips, and anodic reactions in deep, oxygen-deprived areas. Here a strong gradient in
242 oxidizing species can be ruled out, because water was everywhere, including in the crevice. Spatial
243 decoupling could also have been favored by a difference in CPs composition between the crevice and the
244 clay-contacting surfaces. This is the case e.g. in cement grouts, in which localized corrosion correlates
245 with the presence of cathodic magnetite and anodic mackinawite areas [44]. Here, the distribution of
246 sulfide compounds near the clay-steel interface [38] and Fe-(hydr)oxide or silicate (within the crack)
247 actually runs counter to the expected galvanic coupling, thereby further hindering extended crevice
248 corrosion.

249 ***4.2 The effect of partial confinement of pore solution in the liner – overpack*** 250 ***interspace on the heterogeneity of steel corrosion***

251 Our analysis of the time dependence of corrosion interfaces within the CIL specimen, i.e. tube-
252 internal rod space mimicking the liner-overpack interspace, is limited by the fact that only containers
253 reacted for 40 and 76 months were investigated at the microscopic scale. Thus, any evolution from the
254 short-term features can only be speculated from these long-term observations. It is however possible to
255 assess the relative importance of short-term (atmospheric) and long-term aqueous corrosion in the
256 partially confined environment of the liner-overpack interspace. Note that here confined environment

257 refers to relatively stagnant porewater in the interspace because this solution is out of the main stream
258 imposed through the set-up (Figure 2a).

259 Initial corrosion in this interspace is expected to occur by atmospheric oxidation of steel in humid air,
260 at least until all O₂ is captured to form CPs. The amount of CPs that can form can be estimated from the
261 amount of O₂ in the trapped volume and from the simple mass balance of iron oxidation to form
262 magnetite:



264 Although this relationship does not involve water, the presence of water is required under ambient to
265 moderate conditions for corrosion to occur at a significant rate. The residual amount of O₂ in the
266 interspace calculated assuming closure at room temperature approximates 26 μmol. The amount of steel
267 (assumed as pure Fe here for simplicity) that can be oxidized by O₂ is then readily estimated from the
268 volumic mass and the molar mass of iron (about 7.87 g/cm³ and 55.845 g/mol, respectively) and equals
269 about 0.8 mm³. Assuming corrosion is homogeneously distributed over the entire internal surface of steel
270 (i.e. the tube inside walls and the internal rod), the final thickness of corroded iron is thinner than 0.15
271 μm, two orders of magnitude lower than the observed average corrosion depth. The overall fraction of
272 the corrosion damage due to atmospheric corrosion is thus expected to be marginal.

273 Additional insight into the corrosion mechanism can be obtained from the morphology of the
274 corrosion front and the spatial heterogeneities of CPs within the interspace. The internal walls of the tube
275 are notably distinct from the steel-clay interface in terms of morphology of corrosion layers. One key
276 difference is that the nature of the corrosion interface depends on the area location along the inside wall
277 (difference between lower and upper parts). This contrasts with the seemingly random distribution of
278 significantly and sparingly corroded areas over the entire outer surface of the tube (i.e. in direct contact
279 with water-saturated clay) [38]. Second, magnetite and chukanovite predominate in the inside wall and
280 the internal rod DPL, and they are present as massive domains. Silicate CPs also form in the DPL close
281 to the trace of the original steel surface, but the relatively limited proportion does not compare with the
282 thick layers observed at the steel-clay interface [38]. Since all physical (P, T) parameters were identical
283 for the tube inside and outer surfaces, this discrepancy likely reflects distinct chemical and transport

284 conditions in the tube-internal rod interspace. At the steel clay interface (tube outer surface), porewater
285 can react with clay within a few mm from the steel surface, and dissolved elements can then readily
286 diffuse to and from the interface. Stated another way, exchange fluxes between clay and corrosion layers
287 can occur over the entire steel-clay interface, being limited only by diffusion in clay and corrosion layers.
288 In contrast, the interspace solution diffuses through six small holes of about 2 mm in diameter (after
289 diffusion in the nearby clay), hence a total surface of about 19 mm². This is two orders of magnitude
290 smaller than the metal surface in the interspace (about 1500 mm² counting the internal rod and tube
291 inside wall). Given this small ratio, a limited supply of dissolved species such as silicate, Ca or Mg is
292 expected within the interspace compared to the outer steel-clay interface. Part of the Si species observed
293 in the corrosion products may be supplied by the pore water itself, and also by the little amount of clay
294 that dropped through the holes into the interspace. However this supply is probably limited by clay
295 solubility, and by the overall low total surface of minerals. Overall, the formation of all other CPs
296 (except Fe (hydr)oxides) is probably subject to comparable limitations in supply of dissolved elements.

297 Another discrepancy is observed between the bottom and top parts of the tube inner wall. This
298 discrepancy persisted over the exposure time, in spite of full immersion of the inner wall over more than
299 three years. This suggests that the initial differences in early stages of corrosion significantly influence
300 future years and exposure. A possible explanation is that extended corrosion occurred at the lower walls
301 first, somewhat slowing down the flux of water toward the steel surface. Later, as the whole tube was
302 filled, the near-direct contact between steel and solution at the upper part favored the cathodic reaction of
303 water reduction. A galvanic coupling then occurred between the upper and lower parts, resulting in
304 separation between anodic and cathode reactions, and in some protection of the upper walls.

305 Interestingly, steel damage of the tube lower inside wall seems to be of the same order of magnitude
306 (30-40 μm after 76 months) than at the steel-clay interface (average corrosion depths of 29 ± 3 and 43 ±
307 21 μm estimated from gravimetric and direct microscopic measurements, respectively; [38]). This
308 similarity contrasts with the distinct morphologies of corrosion interface. Indeed, at the steel-clay
309 interface, metal-replacing CPs are restricted to several depressions and to a thin (2-3 μm) layer of
310 siderite. In contrast, the tube lower walls are more homogeneously corroded. This suggests that

311 magnetite at the inner wall, however thick, is less protective [45]. The absence of such a thick oxide
312 layer at the steel-clay interface then directly relates to the destabilization of magnetite by silicate [12].

313 Compared to the specimen reacted for 40 months, the most interesting result for the DPL of the 76-
314 month inside wall is the absence of chukanovite. However, because of the confined nature of water in the
315 interspace, it is unclear if similar chemical conditions prevailed in the two specimens at 40 and 76
316 months. In fact, due to the small relative area of the water inlets, small variations in hole permeability
317 (e.g. by clay clogging or corrosion products extension at the holes) would have easily resulted in distinct
318 compositions of the internal solutions. Another evidence for distinct chemical conditions is given by the
319 composition of the siderite layer, which is significantly doped in Ca at 40 months, and not so much at 76
320 months. The absence of chukanovite may also reflect an evolution of the interspace solution toward the
321 magnetite/siderite thermodynamic equilibrium.

322 Finally, our results indicate that the corrosion facies for internal rods at 40 and 76 months are fairly
323 similar, meaning the corrosion rates should be consistent with each other. This expected similarity
324 contrasts with the scatter in the average corrosion depths observed from weight loss measurements.
325 Several hypotheses were examined to explain this discrepancy. Localized corrosion is ruled out, because
326 local SEM cross-sections on genuine specimens and optical observations carried out after desquamation,
327 albeit difficult to interpret, did not reveal any trace of pit-like corrosion. Another hypothesis is a
328 possible high variability in the surface microstructure of the internal rod, due e.g. to different surface
329 pearlite-to-ferrite ratios. In fact, optical and SEM observations on cross-sections suggest that CPs
330 volumes are larger around pearlite islands compared to ferrite grains, suggesting differential corrosion due
331 to some galvanic coupling. Distinct corrosion rates would then relate to distinct pearlite-to-ferrite ratios
332 exposed at the surface from the preparation stage of the specimens (before corrosion). Further
333 investigations are nonetheless required to better understand this discrepancy. Note however that this
334 scatter, though quite significant, may actually account for the variability in overall corrosion damage.

335 **4.3 Implications for the long-term corrosion of steel in deep geological** 336 **environments**

337 The absence of important CPs modifications between 40 and 76 months suggests that the same
338 mechanism operated during this time span, and probably would for longer corrosion times. This implies
339 that a (pseudo-) stationary regime has been attained after 76 months, with the low corrosion rate not
340 expected to increase anymore. Thus the rate laws proposed from the weight loss measurements may be
341 used to provide a rough estimate of the steel damage at 90 °C for anoxic conditions. From equation (2),
342 the average corrosion depth calculated for the internal rod after 10, 100 and 1000 years equal 22 (± 21),
343 202 (± 170), and 2002 (± 1600) μm , respectively. Note that most of the uncertainty derives from the
344 outlier at 40 months. Another value, namely greatest corrosion depth, could be extrapolated from the
345 greatest depths obtained from SEM observations on cross-sections. However, too few data were
346 available to propose any trend, as suggested by the erratic extrema reported here (greatest depths of 100
347 μm after 40 months and 60 μm after 76 months). In addition, no information is available on the
348 propagation kinetics of the oxidation front at these areas, which further hinders any interpretation.
349 Furthermore, it has been shown that the ratio of maximum depth over average damage for anoxic
350 corrosion of C-steel is bounded by a semi-empirical value which steadily decreases over time [46, 47].
351 This upper limit is somewhat corroborated by our results showing little corrosion in the simulated
352 crevice. Note that no trace of actual pitting was observed, minimizing the possibility of local accelerated
353 corrosion that could be critical for the overpack integrity. This lends additional confidence to our
354 extrapolations of average corrosion depths over long times.

355 An additional source of uncertainty is the hypothesis that the system will not evolve much during this
356 long period of time, i.e. has already reached a quasi-stationary regime after 40 or 76 months. Finally,
357 how these corrosion rates obtained under in laboratory-controlled experiments may compare to real in-
358 field (fluctuating) conditions still has to be assessed. For example, a stationary regime suggests that rates
359 of iron corrosion and reactant diffusion in stable geologic environments are not expected to vary much.
360 However, temperature fluctuations in tight geologic systems may occur over only long timescales (years
361 to centuries). A temperature decrease could in fact result in an increase in the corrosion rate as corrosion

362 in such complex systems is controlled by the rates of steel oxidation and CPs precipitation [48].
363 Modelling in pure carbonate systems predicted that the rate of CPs precipitation decreases more rapidly
364 than that of steel oxidation as the temperature decreases towards ambient conditions [48]. Such
365 calculations however do not take into account the diffusion of reactants and products in compact clay,
366 which is usually temperature-activated and can significantly influence the corrosion rate [38].

367 **5 Concluding remarks**

368 Corrosion within simulated crevices and in the liner-overpack interspace (tube inside walls and internal
369 rod) somewhat differs from that of the steel-clay interface. First, areas with the greatest damage are not
370 randomly distributed, but are located essentially where steel is wetted first by porewater. The resulting
371 contrast between areas of extensive and limited corrosion persists even after six years, an indication that
372 subsequent corrosion is controlled by the initial damage. Damage heterogeneity also affects the internal
373 rod in the setup, but to a smaller extent, possibly because the transition from partial to full wetting was
374 more rapid. The DPL is essentially made of magnetite, a mineral which is usually believed to form
375 protective layers at the steel surface. However, here, magnetite coincides with areas of highest damage
376 and presumably has little protective effect. Second, relatively limited amounts of silicate and carbonate
377 solids have formed in the interspace, compared to the extensive amounts present at the steel-clay
378 interface. Because the systems are subject to homogeneous pressure and temperature conditions, this
379 contrast can be explained only by lower solution concentrations of elements (Si, Ca) in this interspace.

380 In spite of these spatial heterogeneities, the greatest sample damage after six years remains significantly
381 smaller than values measured in the porewater [28, 29], attesting to surface protection, and compares
382 with what was found for steel-clay compact interfaces. This is probably because diffusion, either through
383 the tube holes or in the bulk clay, significantly limits the transport of reactants toward corrosion sites.
384 Thus it seems that limiting water fluxes is key to limiting steel corrosion, even in the presence of
385 fluctuations in water content, composition, and temperature.

386 **6 Acknowledgements**

387 The authors gratefully acknowledge the financial support of Andra and EDF for experimental work
388 and results interpretation. D. Crusset, F. Foct, J.M. Gras and members of the GL “Verre-Fer-Argile” are
389 also gratefully acknowledged for fruitful discussions on the setup definition and on scientific results.
390 Claude Gatabin is thanked for extraction the samples from the high-pressure cells. The fruitful
391 contribution of three anonymous reviewers is acknowledged.

392 **Data availability**

393 The raw/processed data required to reproduce these findings cannot be shared at this time due to legal
394 reasons.

395 **Declaration of interest**

396 The authors declare no conflict of interest.

397 **References**

- 398 [1] G. De Marsily, E. Ledoux, A. Barbreau, J. Margat, Nuclear waste disposal: can the geologist
399 guarantee isolation?, *Science*, 197 (1977) 519-527.
- 400 [2] K.B. Krauskopf, Aqueous geochemistry of radioactive waste disposal, *Appl. Geochem.*, 1 (1986)
401 15-23.
- 402 [3] M. Sawiki, Council Directive 2011/70/EURATOM of 19 July 2011 establishing a Community
403 framework for the responsible and safe management of spent fuel and radioactive waste, *Off. J.*
404 *Europ. Union*, 199 (2011) 48-56.
- 405 [4] F. King, Waste containers, in: T.R. Allen, R.E. Stoller, S. Yamanaka (Eds.) *Material performance*
406 *and corrosion waste materials*, Elsevier, Amsterdam, 2012, pp. 421-450.
- 407 [5] F. King, Container materials for the storage and disposal of nuclear waste, *Corrosion*, 69 (2013)
408 986-1011.
- 409 [6] Andra, Evaluation de la faisabilité du stockage géologique en formation argileuse, in, Andra,
410 Chatenay-Malabry, France, 2005, pp. 240.
- 411 [7] F.T. Madsen, Clay mineralogical investigations related to nuclear waste disposal, *Clay Min.*, 33
412 (1998) 109-129.
- 413 [8] L. Carlson, O. Karnland, V.M. Oversby, A.P. Rance, N.R. Smart, M. Snellman, M. Vahanen, L.O.
414 Werme, Experimental studies of the interactions between anaerobically corroding iron and
415 bentonite, *Phys. Chem. Earth*, 32 (2007) 334-345.
- 416 [9] N.R. Smart, A.P. Rance, L.O. Werme, The effect of radiation on the anaerobic corrosion of steel, *J.*
417 *Nucl. Mater.*, 379 (2008) 97-104.
- 418 [10] C. Bataillon, C. Musy, M. Roy, Corrosion des surconteneurs de déchets, cas d'un surconteneur
419 en acier faiblement allié., *J. Phys. IV*, 11 (2001) 267-274.
- 420 [11] F.A. Martin, C. Bataillon, M.L. Schlegel, Corrosion of iron and low alloyed steel within a water
421 saturated brick of clay under anaerobic deep geological disposal conditions: An integrated
422 experiment, *J. Nucl. Mater.*, 379 (2008) 80-90.
- 423 [12] M.L. Schlegel, C. Bataillon, K. Benhamida, C. Blanc, D. Menut, J.-L. Lacour, Metal corrosion and
424 argillite transformation at the water-saturated, high temperature iron-clay interface: a
425 microscopic-scale study, *Appl. Geochem.*, 23 (2008) 2619-2633.
- 426 [13] M.L. Schlegel, C. Bataillon, C. Blanc, D. Prêt, E. Foy, Anodic activation of iron corrosion in clay
427 media under water-saturated conditions at 90 °C: characterization of the corrosion interface,
428 *Environ. Sci. Technol.*, 44 (2010) 1503-1508.
- 429 [14] G. de Combarieu, P. Barboux, Y. Minet, Iron corrosion in Callovo-Oxfordian argillite: From
430 experiments to thermodynamic/kinetic modelling, *Phys. Chem. Earth*, 32 (2007) 346-358.
- 431 [15] G. de Combarieu, M.L. Schlegel, D. Neff, E. Foy, D. Vantelon, P. Barboux, S. Gin, Glass-Iron-Clay
432 interaction in a radioactive waste geological disposal: an integrated laboratory-scale experiment,
433 *Appl. Geochem.*, 26 (2011) 65-79.
- 434 [16] Y. El Mendili, A. Abdelouas, J.F. Bardeau, Insight into the mechanism of carbon steel corrosion
435 under aerobic and anaerobic conditions, *Phys. Chem. Chem. Phys.*, 15 (2013) 9197-9204.
- 436 [17] Y. El Mendili, A. Abdelouas, J.F. Bardeau, Impact of a sulphidogenic environment on the
437 corrosion behavior of carbon steel at 90°C, *RSC Adv.*, 3 (2013) 15148-15156.

- 438 [18] Y. El Mendili, A. Abdelouas, A.A. Chaou, J.F. Bardeau, M.L. Schlegel, Carbon steel corrosion in
439 clay-rich environment, *Corros. Sci.*, 88 (2014) 56-65.
- 440 [19] Y. El Mendili, A. Abdelouas, G. Karakurt, A.A. Chaou, R. Essehli, J.F. Bardeau, J.M. Greneche, The
441 effect of temperature on carbon steel corrosion under geological conditions, *Appl. Geochem.*, 52
442 (2015) 76-85.
- 443 [20] S. Kaufhold, A.W. Hassel, D. Sanders, R. Dohrmann, Corrosion of high-level radioactive waste
444 iron-canisters in contact with bentonite, *J. Hazard. Mater.*, 285 (2015) 464-473.
- 445 [21] S. Kaufhold, R. Dohrmann, Distinguishing between more and less suitable bentonites for storage
446 of high-level radioactive waste, *Clay Min.*, 51 (2016) 289-302.
- 447 [22] Y. Leon, M. Saheb, E. Drouet, D. Neff, E. Foy, E. Leroy, J.J. Dynes, P. Dillmann, Interfacial layer on
448 archaeological mild steel corroded in carbonated anoxic environments studied with coupled
449 micro and nano probes, *Corros. Sci.*, 88 (2014) 23-35.
- 450 [23] M. Robineau, A. Romaine, R. Sabot, M. Jeannin, V. Deydier, S. Necib, P. Refait, Galvanic
451 corrosion of carbon steel in anoxic conditions at 80 °C associated with a heterogeneous
452 magnetite (Fe₃O₄)/mackinawite (FeS) layer, *Electrochim. Acta*, 255 (2017) 274-285.
- 453 [24] A. Romaine, M. Jeannin, R. Sabot, S. Necib, P. Refait, Corrosion processes of carbon steel in
454 argillite: Galvanic effects associated with the heterogeneity of the corrosion product layer,
455 *Electrochim. Acta*, 182 (2015) 1019-1028.
- 456 [25] S. Necib, N. Diomidis, P. Keech, M. Nakayama, Corrosion of carbon steel in clay environments
457 relevant to radioactive waste geological disposals, Mont Terri rock laboratory (Switzerland), *Swiss*
458 *J. Geosci.*, 110 (2017) 329-342.
- 459 [26] S. Necib, Y. Linard, D. Crusset, M. Schlegel, S. Daumas, N. Michau, Corrosion processes of C-steel
460 in long-term repositories conditions, *Corr. Eng. Sci. Technol.*, 52 (2017) 127-130.
- 461 [27] S. Necib, Y. Linard, D. Crusset, N. Michau, S. Daumas, E. Burger, A. Romaine, M.L. Schlegel,
462 Corrosion at the carbon steel-clay borehole water and gas interfaces at 85°C under anoxic and
463 transient acidic conditions, *Corros. Sci.*, 111 (2016) 242-258.
- 464 [28] M.L. Schlegel, S. Necib, S. Daumas, C. Blanc, E. Foy, N. Trcera, A. Romaine, Microstructural
465 characterization of carbon steel corrosion in clay borehole water, under anoxic and transient
466 acidic conditions, *Corros. Sci.*, 109 (2016) 126-144.
- 467 [29] M.L. Schlegel, S. Necib, S. Daumas, M. Labat, C. Blanc, E. Foy, Y. Linard, Corrosion at the carbon
468 steel-clay borehole water and gas interfaces at 85 °C under anoxic alkaline conditions, *Corros.*
469 *Sci.*, 136 (2018) 70-90.
- 470 [30] D. Neff, P. Dillmann, L. Bellot-Gurlet, G. Berranger, Corrosion of iron archaeological artefacts in
471 soil : characterisation of the corrosion system, *Corros. Sci.*, 47 (2005) 515-535.
- 472 [31] D. Neff, P. Dillmann, M. Descostes, G. Beranger, Corrosion of iron archaeological artefacts in
473 soil: Estimation of the average corrosion rates involving analytical techniques and
474 thermodynamic calculations, *Corros. Sci.*, 48 (2006) 2947-2970.
- 475 [32] D. Neff, M. Saheb, J. Monnier, S. Perrin, M. Descostes, V. L'Hostis, D. Crusset, A. Millard, P.
476 Dillmann, A review of the archaeological analogue approaches to predict the long-term corrosion
477 behaviour of carbon steel overpack and reinforced concrete structures in the French disposal
478 systems, *J. Nucl. Mater.*, 402 (2010) 196-205.

- 479 [33] D. Neff, E. Vega, P. Dillmann, M. Descostes, L. Bellot-Gurlet, G. Beranger, Contribution of iron
480 archeological artefacts to the estimation of average corrosion rates and the long-term corrosion
481 mechanisms of low-carbon steel buried in soils, in: P. Dillmann, G. Beranger, P. Piccardo, H.
482 Matthiesen (Eds.) Corrosion of metallic heritage artefacts, Woodhead, Cambridge, UK, 2007, pp.
483 41-76.
- 484 [34] M. Saheb, D. Neff, P. Dillmann, H. Matthiesen, E. Foy, Long-term corrosion behaviour of low-
485 carbon steel in anoxic environment: characterization of archaeological artefacts, *J. Nucl. Mater.*,
486 379 (2008) 118-123.
- 487 [35] M. Saheb, M. Descostes, D. Neff, H. Matthiesen, A. Michelin, P. Dillmann, Iron corrosion in an
488 anoxic soil: Comparison between thermodynamic modelling and ferrous archaeological artefacts
489 characterised along with the local in situ geochemical conditions, *Appl. Geochem.*, 25 (2010)
490 1937-1948.
- 491 [36] M. Saheb, D. Neff, L. Bellot-Gurlet, P. Dillmann, Raman study of a deuterated iron
492 hydroxycarbonate to assess long-term corrosion mechanisms in anoxic soils, *J. Raman Spectrosc.*,
493 42 (2011) 1100-1108.
- 494 [37] G.A. Yakovlev, A.V. Chukin, V.I. Grokhovsky, V.A. Semionkin, M.I. Oshtrakh, Study of Dronino
495 iron meteorite weathering in clay sand using Mossbauer spectroscopy, *Croatica Chemica Acta*, 89
496 (2016) 117-124.
- 497 [38] M.L. Schlegel, F. Martin, M. Fenart, C. Blanc, J. Varlet, E. Foy, D. Pret, N. Trcera, Corrosion at the
498 carbon steel-clay compact interface at 90°C: insight into short- and long-term corrosion facies,
499 *Corros. Sci.*, 152 (2019) 31-44.
- 500 [39] F. Martin, S. Perrin, M. Fenart, M. Schlegel, C. Bataillon, On corrosion of carbon steels in
501 Callovo-Oxfordian clay: complementary EIS, gravimetric and structural study providing insights on
502 long term behaviour in French geological disposal conditions, *Corr. Eng. Sci. Technol.*, 49 (2014)
503 460-466.
- 504 [40] T. Ishidera, K. Ueno, S. Kurosawa, T. Suyama, Investigation of montmorillonite alteration and
505 form of iron corrosion products in compacted bentonite in contact with carbon steel for ten
506 years, *Phys. Chem. Earth*, 33 (2008) S269-S275.
- 507 [41] M.K. Nieuwoudt, J.D. Comins, I. Cukrowski, The growth of the passive film on iron in 0.05 M
508 NaOH studied in situ by Raman microspectroscopy and electrochemical polarization. Part II: In
509 situ Raman spectra of the passive film surface during growth by electrochemical polarization, *J.*
510 *Raman Spectrosc.*, 42 (2011) 1353-1365.
- 511 [42] M.K. Nieuwoudt, J.D. Comins, I. Cukrowski, The growth of the passive film on iron in 0.05 M
512 NaOH studied in situ by Raman micro-spectroscopy and electrochemical polarisation. Part I: near-
513 resonance enhancement of the Raman spectra of iron oxide and oxyhydroxide compounds, *J.*
514 *Raman Spectrosc.*, 42 (2011) 1335-1339.
- 515 [43] C.S. Brossia, G.A. Cragnolino, Effect of environmental variables on localized corrosion of carbon
516 steel, *Corrosion*, 56 (2000) 505-514.
- 517 [44] M. Robineau, R. Sabot, M. Jeannin, V. Deydier, D. Crusset, P. Refait, Mechanisms of localized
518 corrosion of carbon steel associated with magnetite/mackinawite layers in a cement grout,
519 *Mater. Corros.*, senqsensen (2020) 1-17.

520 [45] C. Bataillon, F. Bouchon, C. Chainais-Hillairet, C. Desgranges, E. Hoarau, F. Martin, S. Perrin, M.
521 Tupin, J. Talandier, Corrosion modelling of iron based alloy in nuclear waste repository,
522 Electrochim. Acta, 55 (2010) 4451-4467.

523 [46] J.-M. Gras, Life prediction for HLW containers - issues related to long-term extrapolation of
524 corrosion resistance, C.R. Physique, 3 (2002) 891-902.

525 [47] F. Foct, J.M. Gras, Semi-empirical model for carbon steel corrosion in long term geological
526 nuclear waste disposal, in: International Workshop "Prediction of long term corrosion behaviour
527 in nuclear waste systems", EFC, Cadarache, France, 2002.

528 [48] S. Nešić, M. Nordsveen, R. Nyborg, A. Stangeland, A mechanistic model for carbon dioxide
529 corrosion of mild steel in the presence of protective iron carbonate films - Part 2: A numerical
530 experiment, Corrosion, 59 (2003) 489-497.

531

532 **7 Figure captions**

533 Figure 1. (a) Schematic cross-section of the former design for disposal cells in the French High-level
534 waste repository. (b) Illustration of the gradual filling of the space between clay and the liner. (c)
535 Illustration of the confined interspace between the liner and the overpack, resulting in corrosion
536 under confined conditions.

537 Figure 2. (a) Schematic illustration of the high-pressure cell setup and positioning of the samples. In
538 real experiments, “crevice” and “cover integrity loss” (CIL) specimens were corroded in separate
539 cells. (b) Illustration of the sample geometries.

540 Figure 3. Sample damage as a function of reaction time for the massive half-rods of the simulated
541 crevices (a) and the steel rods within the CIL specimens (b). Also illustrated are the fits of
542 experimental data with logarithmic law, power law and linear law.

543 Figure 4. Scanning electron images (BSE mode) showing the evolution of the corrosion interfaces in
544 the simulated crevices as a function of reaction time. (a,b) C07 sample, 7 months. (c) C13, 13
545 months. (d) C27, 27 months. (e) C40, 40 months. (f) C76, 76 months.

546 Figure 5. (a) Chemical mapping of element distributions at the simulated crevice interface of the C40
547 rod (40 months of reaction). The dotted line marks the interface between inner and outer
548 corrosion layers. (b) μ XRD diagram of a thin slice of the simulated crevice.

549 Figure 6. (a) Optical images of the two envelopes and internal rods of the CIL specimens after 15
550 months of reaction time, showing the presence of water marks indicating gradual filling of
551 porewater inside the envelope.

552 Figure 7. Scanning electron micrographs of the corrosion interfaces in the CIL setup for 40 (a-c) and
553 76 (d-f) months of reaction time. (a,d) Lower inside wall of the tube. (b,e) Central rod.

554 Figure 8. (a) BSE image and chemical mapping of element distributions at the lower inside wall of the
555 CIL setup corroded for 40 months. DPL: dense products layer. MCL: median corrosion layer.

556 OCPs: outer corrosion products. (b) μ Raman spectra at selected points of interest (PI) of the
557 corrosion interface. The PI locations are indicated on the BSE image.

558 Figure 9. (a) BSE image and chemical mapping of element distributions at the upper inside wall of the
559 CIL setup corroded for 40 months.

560 Figure 10. (a) BSE image and chemical mapping of element distributions for the corrosion interface of
561 the central rod for the CIL setup corroded for 40 months. (b) μ Raman spectra at selected points
562 of interest (PI) of the corrosion interface. The PI locations are indicated on the BSE image.

563

564 **8 Tables**

565

566

Table 1. List of the samples investigated in this study.

Name	Reaction time	Sample type
C07	7 months	Crevice
C13	13 months	Crevice
C27	27 months	Crevice
C40	40 months	Crevice
T40	40 months	Tube + internal rod
C76	76 months	Crevice
T76	76 months	Tube + internal rod

567

568

Table 2. Quantification of SEM-EDX analyses for the artificial crevice of the C40 sample (40 months). The PI are indicated in Figure 5a.

Analysis spot	Composition (at. %)											
	O	Na	Mg	Al	Si	S	Cl	K	Ca	Fe	Cu	Zn
1	59.1	0.3	0.3	0.2	14.8	1.4	0.1	0.0	0.1	23.3	0.2	0.0
2	58.0	0.2	0.3	0.1	11.0	1.4	0.1	0.0	0.2	28.5	0.2	0.0
3	58.4	0.1	0.4	0.2	14.7	1.1	0.0	0.0	0.4	24.4	0.2	0.0
4	68.2	0.2	0.8	0.1	0.2	0.0	0.0	0.0	3.0	27.0	0.3	0.1
5	71.0	0.3	1.1	0.1	0.2	0.1	0.0	0.0	3.4	23.2	0.4	0.1
6	71.4	0.3	1.6	0.2	0.4	0.3	0.0	0.0	4.6	20.7	0.5	0.2

569

570

571

Table 3. Quantification of SEM-EDX analyses at the lower inside wall of the CIL setup reacted for 40 months. The PI are indicated in Figure 8a.

PI spot	Composition (at. %)									
	O	Na	Mg	Al	Si	S	Cl	K	Ca	Fe
1	53.6	0.2	0.3	0.2	0.6	0.4	0.0	0.0	0.1	44.5
2	55.2	0.3	0.4	0.3	3.3	0.2	0.0	0.0	0.0	40.2
3	62.1	0.4	0.4	0.2	0.6	1.2	0.0	0.0	0.1	34.9
4	62.8	0.4	0.4	0.3	1.9	1.1	0.0	0.1	0.1	33.0
5	60.7	0.4	0.5	0.3	17.4	0.5	0.3	0.0	0.1	19.8
6	52.1	0.1	0.4	0.3	19.6	0.6	0.2	0.0	0.0	26.8
7	54.1	0.2	0.3	0.2	1.8	0.2	0.4	0.0	0.2	42.5
8	51.5	0.2	0.4	0.2	2.1	0.3	0.5	0.0	0.2	44.6

572

573

574

575

Table 4. Quantification of SEM-EDX analyses at the upper inside wall of the CIL setup corroded for 40 months. The PI are indicated in Figure 9.

Analysis spot	Composition (at. %)									
	O	Na	Mg	Al	Si	S	Cl	K	Ca	Fe
1	49.9	0.1	0.2	0.1	0.8	0.3	0.1	0	0	48.53
2	55.6	0.1	0.4	0.2	17.6	0.5	0.1	0	0	25.38
3	54.9	0.2	0.4	0.3	17.4	0.8	0.1	0	0.1	25.69
4	51.2	0	0.3	0.3	18.9	0.7	0.1	0	0.2	28.34
5	60.7	0	0.3	0.1	0.2	0.1	0	0	0.3	38.26
6	65.1	0.2	0.5	0.1	0.2	0.1	0	0	0.5	33.35
7	63.4	0.2	1.3	0.2	0.2	0.1	0.1	0	4.9	29.78
8	66.6	0.3	1.3	0.2	0.2	0	0	0	3.9	27.51
9	69.6	0.6	0.7	0.3	0.2	0	0	0	0.6	27.98
10	62.3	0	0.3	0.1	0.3	0.1	0	0	0.7	36.24
11	53.8	0.3	0.4	0.2	2.4	0.2	0.1	0	0.1	42.5

576

577

578

Table 5. Quantification of SEM-EDX analyses at the corrosion interface of the internal rod in the CIL setup. The PI are indicated in Figure 10a.

PI	Composition (at. %)										
	O	Na	Mg	Al	Si	S	Cl	K	Ca	Fe	Cu
1	58.4	0.5	0.4	0.2	0.4	0.3	0	0.0	0	39.0	0.7
2	67.0	0.7	0.5	0.2	1.0	0.9	0	0	0.1	28.9	0.7
3	56.8	0.2	0.3	0.2	17.5	0.7	0.1	0	0.1	23.9	0.2
4	54.7	0.0	0.4	0.2	14.8	0.5	0.1	0	0	29.3	0.0
5	65.8	0.7	0.5	0.2	0.4	0.8	0.1	0	0.1	30.8	0.7
6	64.9	0.3	0.7	0.1	0.3	0.2	0	0.1	5.9	27.1	0.3
7	70.6	0.4	0.5	0.1	0.1	0	0	0.1	0.4	27.2	0.4
8	72.9	0.4	1.1	0.3	0.4	0.2	0	0	6.8	17.5	0.4
9	59.5	0.8	0.6	0.3	0.9	0.6	0.5	0	0.1	35.9	0.8

579

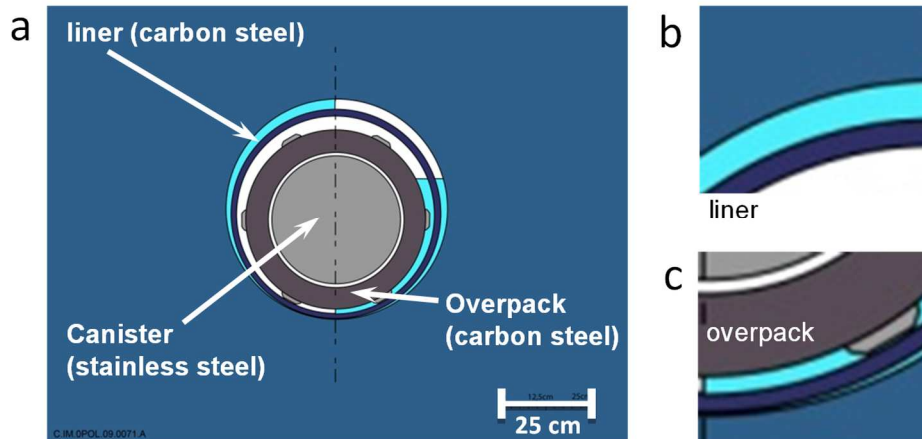
580

581

582

Figures

583



584

585

586 Figure 1. (a) Schematic cross-section of the former design for disposal cells in the French High-level
587 waste repository. (b) Illustration of the gradual filling of the space between clay and the liner. (c)
588 Illustration of the confined interspace between the liner and the overpack, resulting in corrosion
589 under confined conditions.

590

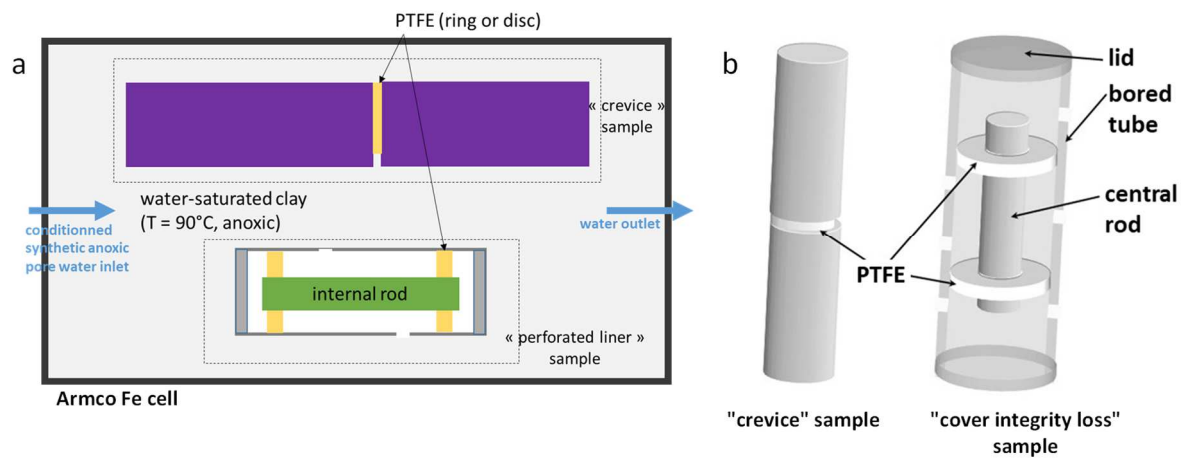
591

592

593

594

595



596

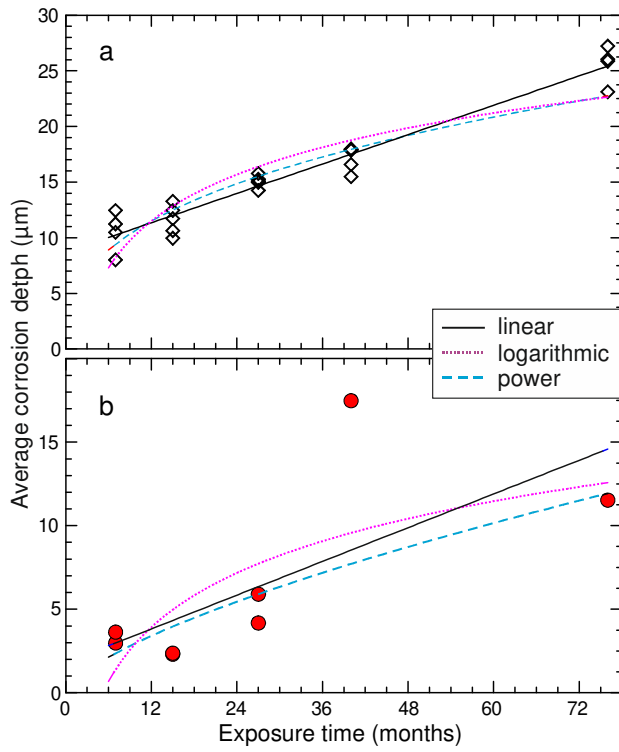
597

598 Figure 2. (a) Schematic illustration of the high-pressure cell setup and positioning of the samples. In
599 real experiments, "crevice" and "cover integrity loss" (CIL) specimens were corroded in separate
600 cells. (b) Illustration of the sample geometries.

601

602

603

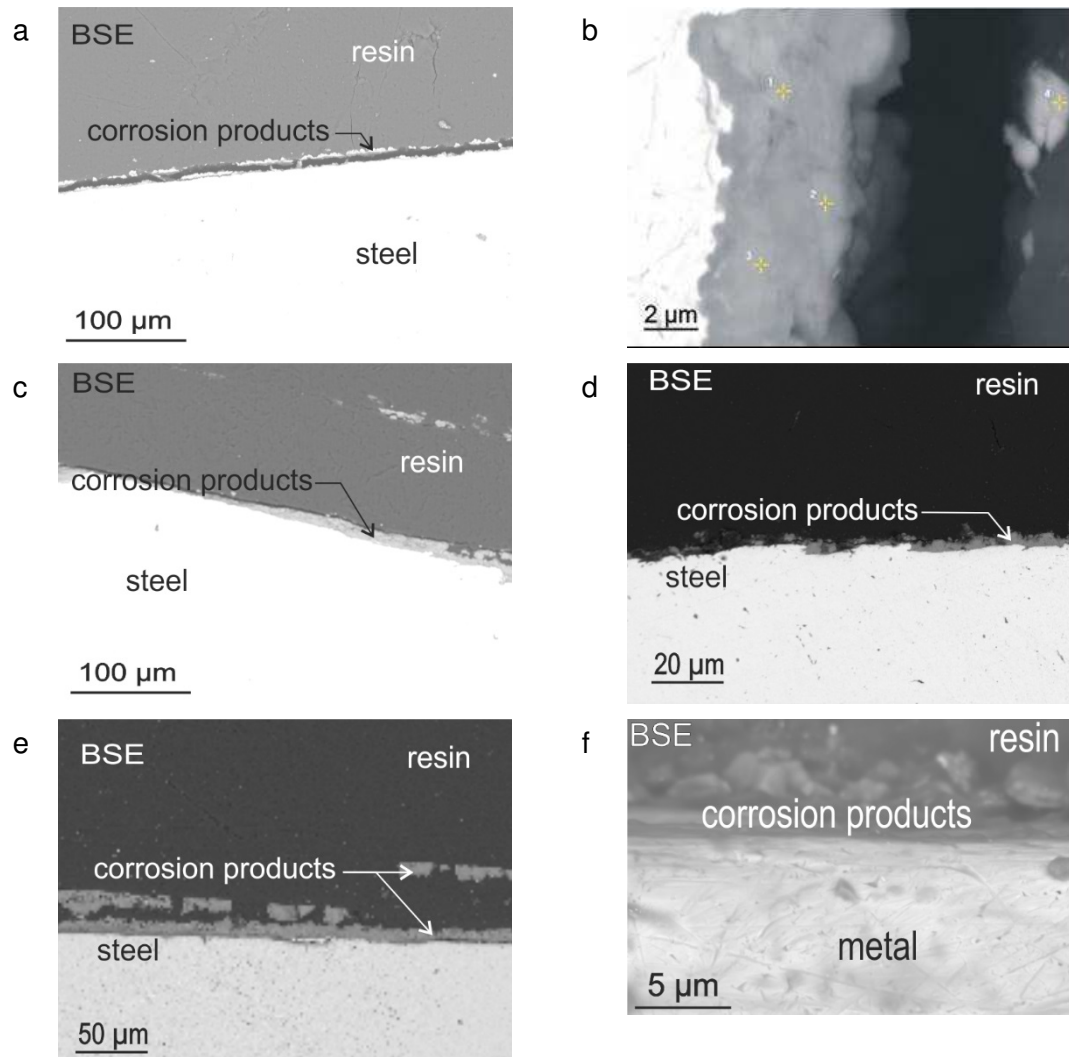


604

605

606 Figure 3. Sample damage as a function of reaction time for the massive half-rods of the simulated
 607 crevices (a) and the steel rods within the CIL specimens (b). Also illustrated are the fits of
 608 experimental data with logarithmic law, power law and linear law.

609



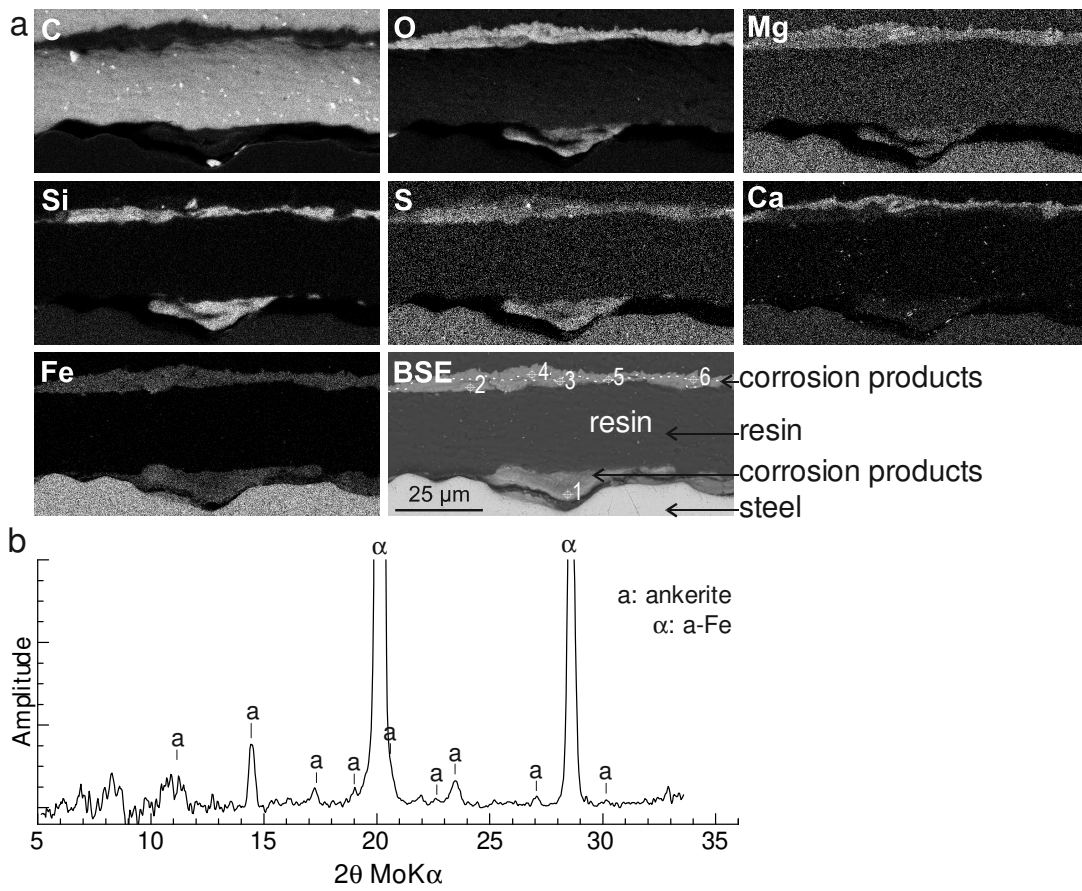
610

611 Figure 4. Scanning electron images (BSE mode) showing the evolution of the corrosion interfaces in
 612 the simulated crevices as a function of reaction time. (a ,b) C07 sample, 7 months. (c) C13, 13
 613 months. (d) C27, 27 months. (e) C40, 40 months. (f) C76, 76 months.

614

615

616

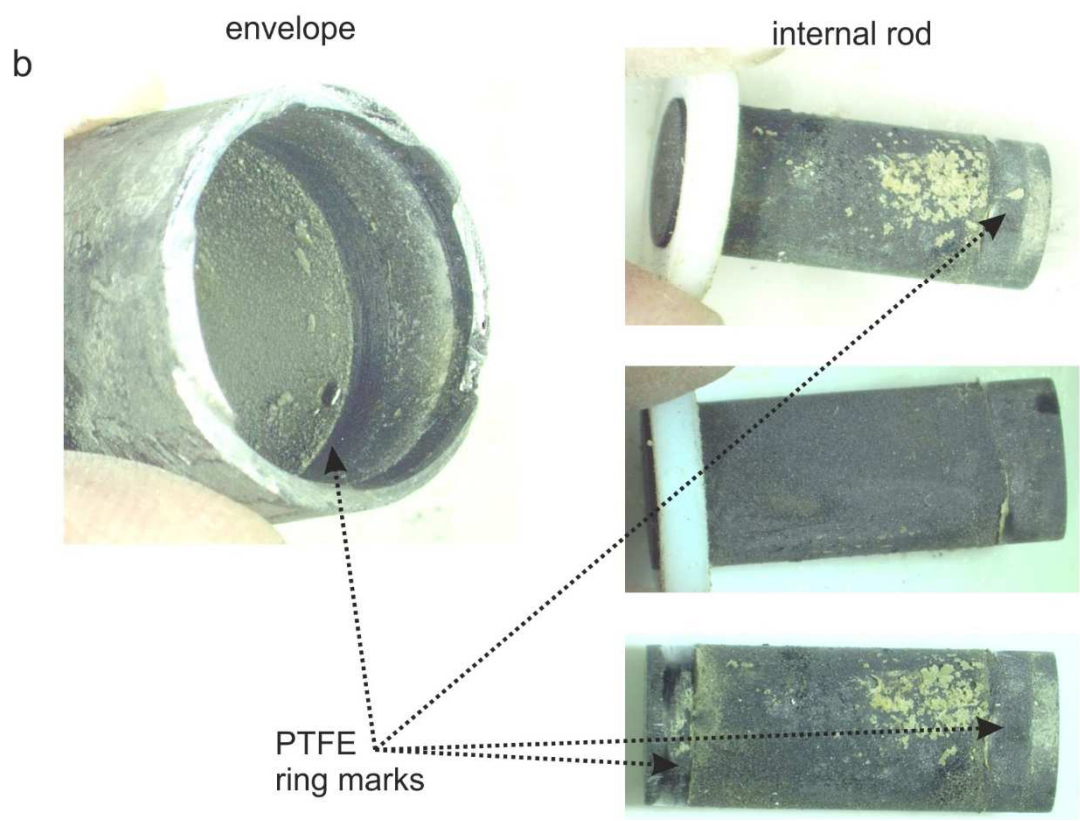
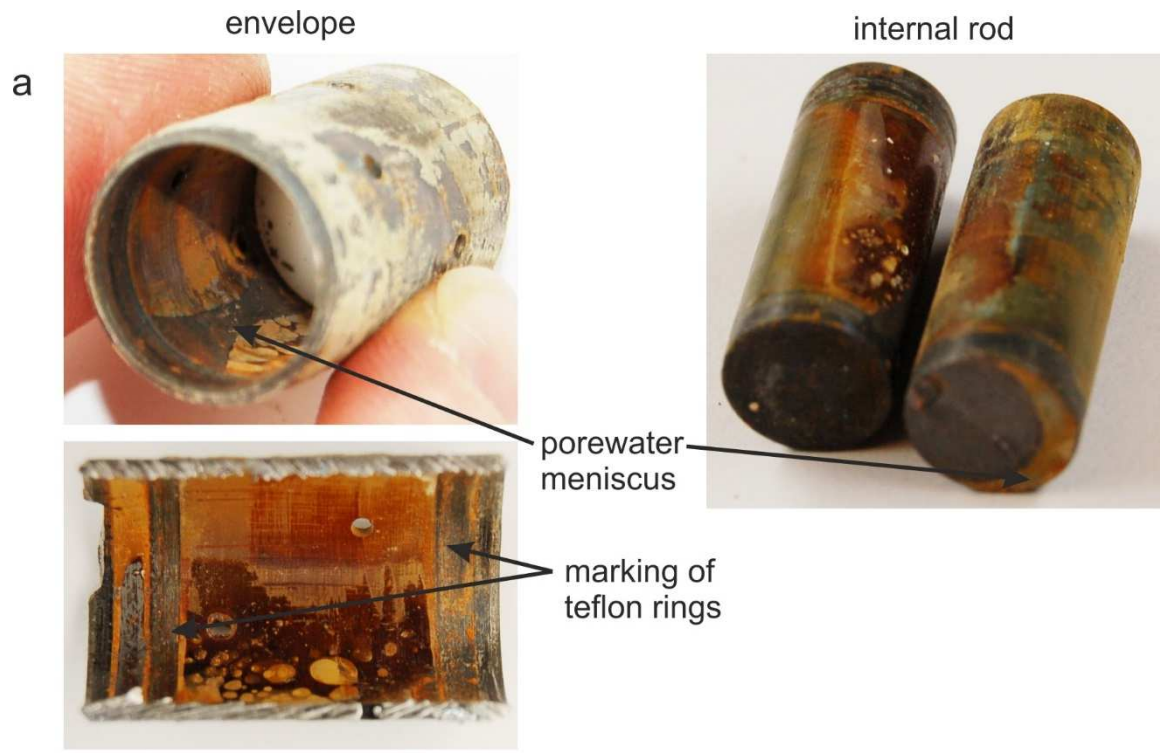


617

618

619 Figure 5. (a) Chemical mapping of element distributions at the simulated crevice interface of the C40
620 rod (40 months of reaction). The dotted line marks the interface between inner and outer
621 corrosion layers. (b) μ XRD diagram of a thin slice of the simulated crevice.

622

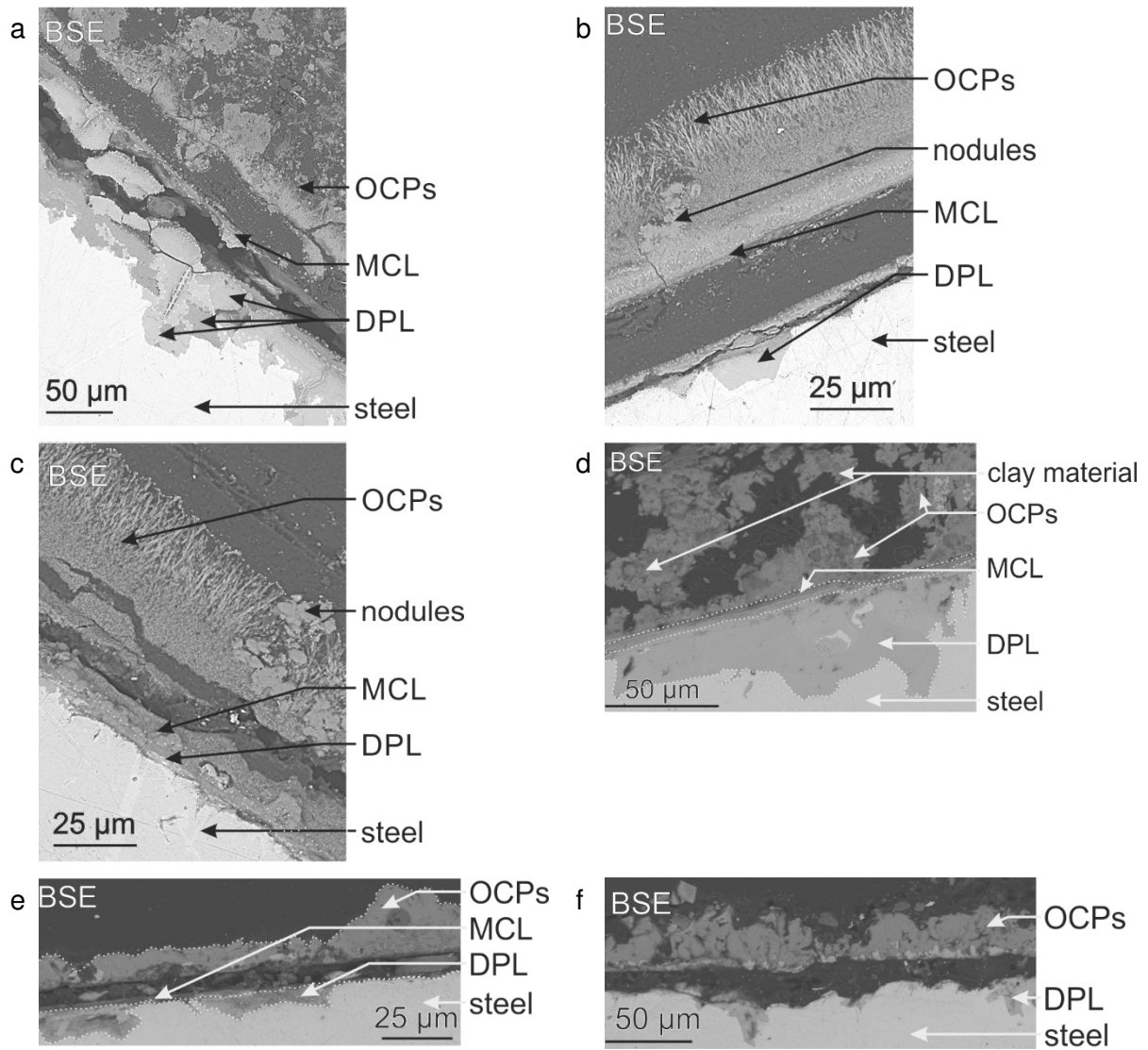


623
624
625
626
627
628

Figure 6. (a) Optical images of the two envelopes and internal rods of the CIL specimens after 15 months of reaction time, showing the presence of water marks indicating gradual filling of porewater inside the envelope. (b) Optical images of the two envelopes and internal rods of the CIL specimens after 76 months of reaction time.

629

630

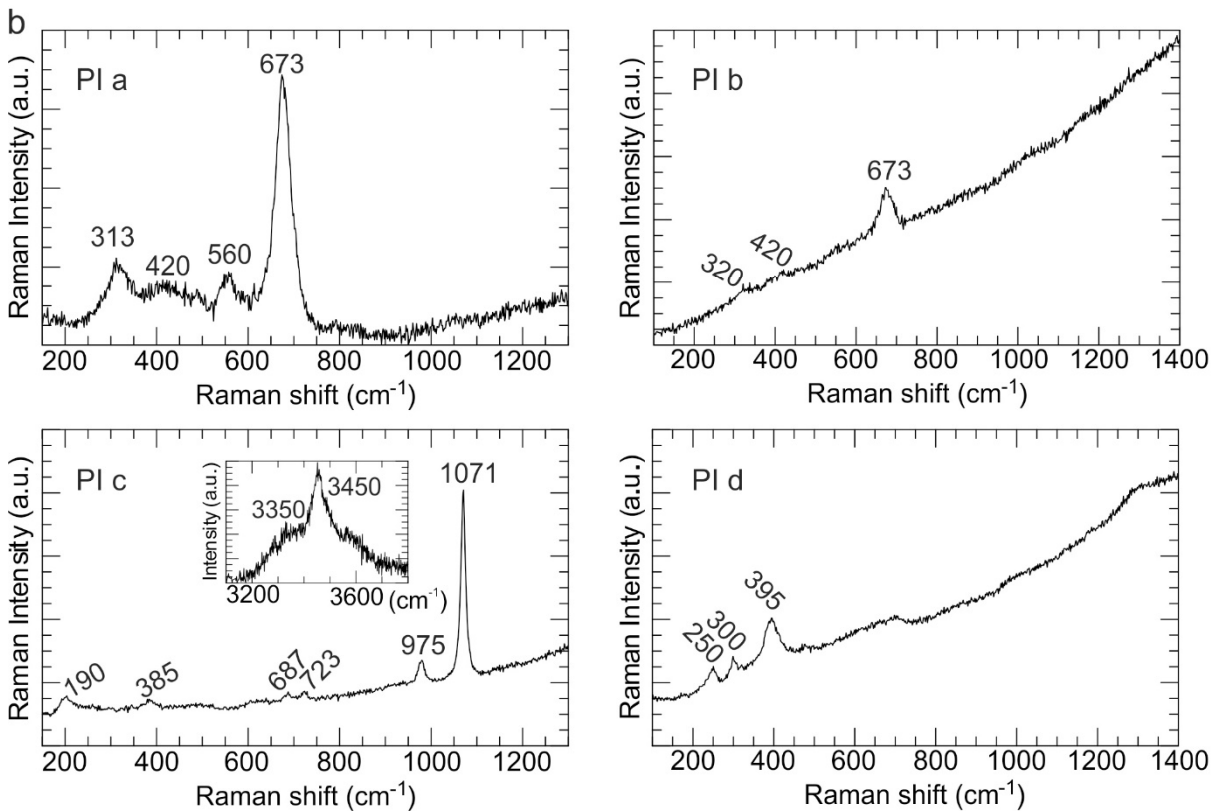
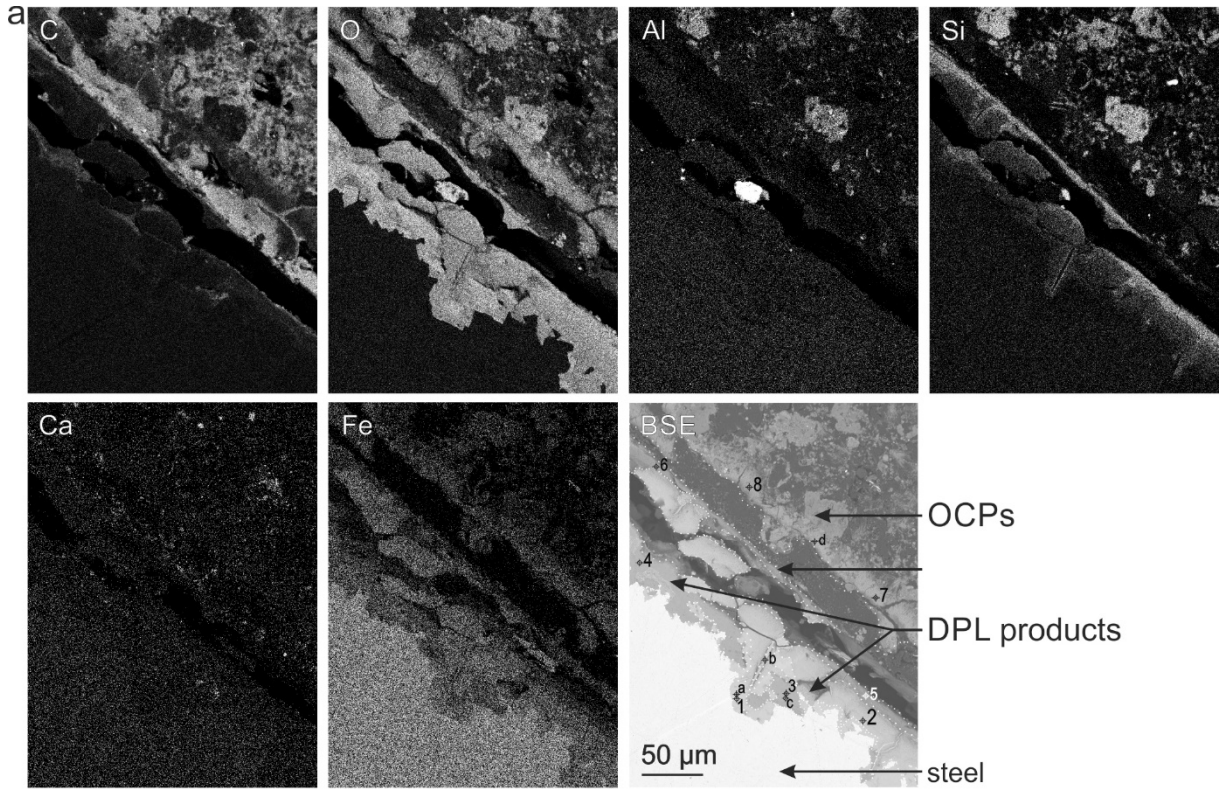


631

632 Figure 7. Scanning electron micrographs of the corrosion interfaces in the CIL setup for 40 (a-c) and
633 76 (d-f) months of reaction time. (a,d) Lower inside wall of the tube. (b,e) Central rod. (c,f) Upper
634 inside wall of the tube. DPL: dense products layer. MCL: median corrosion layer. OCPs: outer
635 corrosion products.

636

637

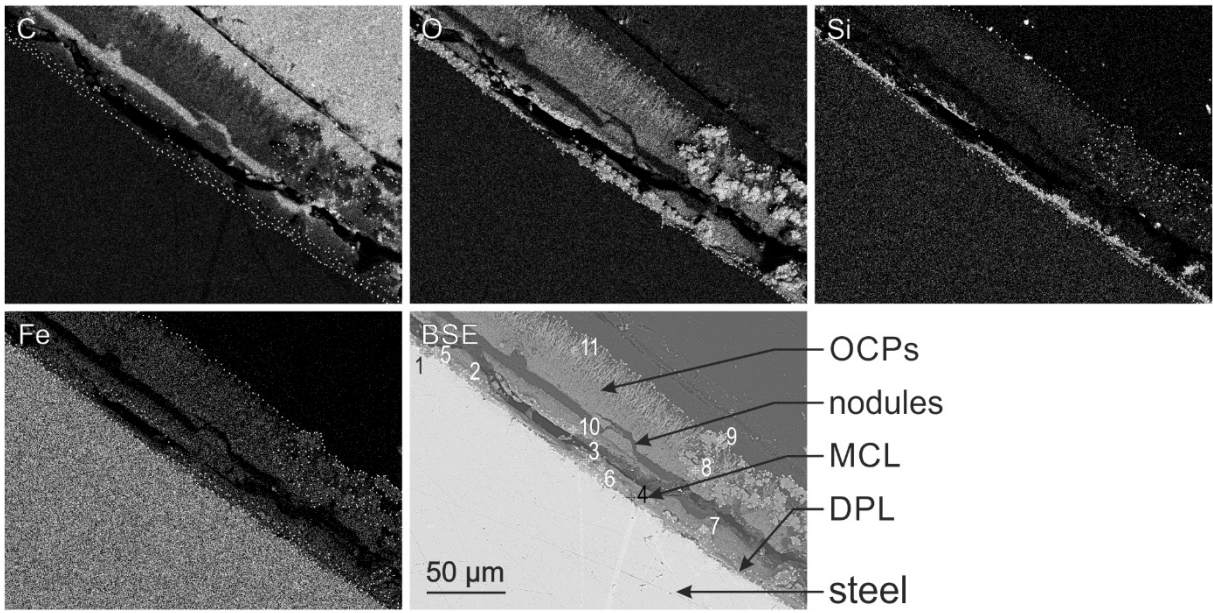


638

639 Figure 8. (a) BSE image and chemical mapping of element distributions at the lower inside wall of the
 640 CIL setup corroded for 40 months. DPL: dense products layer. MCL: median corrosion layer. OCPs:
 641 outer corrosion products. (b) μ Raman spectra at selected points of interest (PI) of the corrosion
 642 interface. The PI locations are indicated on the BSE image.

643

644



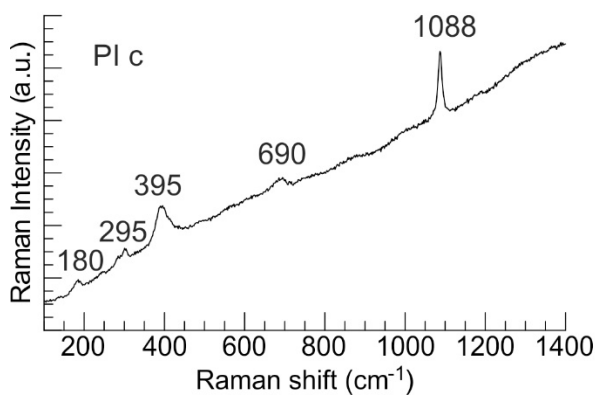
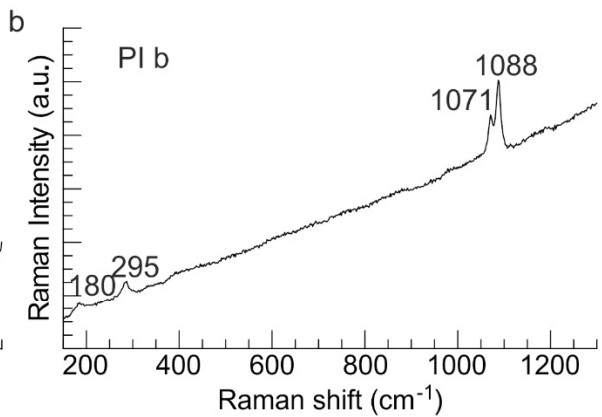
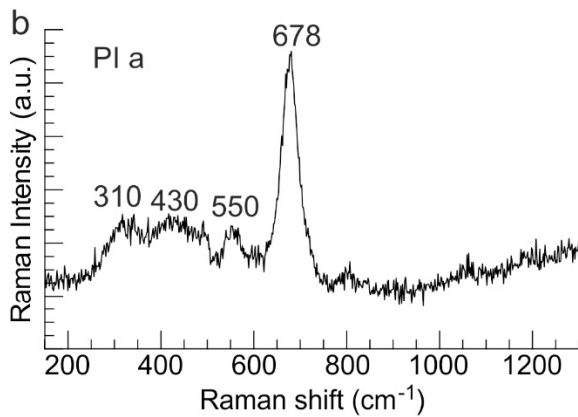
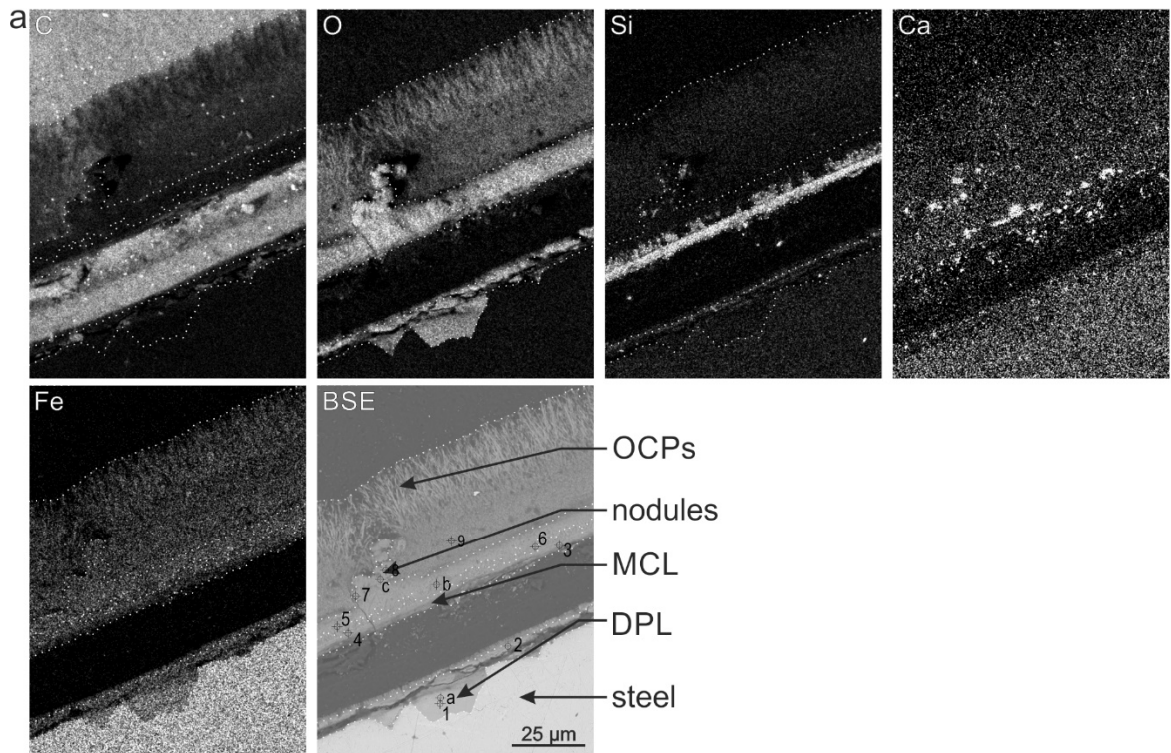
645

646 Figure 9. (a) BSE image and chemical mapping of element distributions at the upper inside wall of
647 the CIL setup corroded for 40 months.

648

649

650



651

652 Figure 10. (a) BSE image and chemical mapping of element distributions for the corrosion interface
 653 of the central rod for the CIL setup corroded for 40 months. (b) μ Raman spectra at selected
 654 points of interest (PI) of the corrosion interface. The PI locations are indicated on the BSE image.